Freestanding 2D metal oxides at the single-atomic-layer limit

Meng Gao[1#], Deping Guo[2,3#], Ang Li[1#], Renhong Wang[2,3#], Zhitong Jin[4], Yuhao Pan[2], Jiuxiang Dai[4], Panqi Huang[4], Kangjie Liu[4], Lin Zhou[4], Stephen J. Pennycook[1]*, Wei Ji[2,3]*, Wu Zhou[1]*

[1]School of Physical Sciences, University of Chinese Academy of Sciences, Beijing 100049, China

[2]Beijing Key Laboratory of Optoelectronic Functional Materials and Micro-Nano Devices, School of Physics, Renmin University of China, Beijing 100872, China

[3]Key Laboratory of Quantum State Construction and Manipulation (Ministry of Education), Renmin University of China, Beijing 100872, China

[4]School of Chemistry and Chemical Engineering, Shanghai Jiao Tong University, Shanghai 200240, China

[#] These authors contributed equally: Meng Gao, Deping Guo, Ang Li, Renhong Wang.

* Corresponding authors: wuzhou@ucas.ac.cn (W.Z.); wji@ruc.edu.cn (W.J.); stevepennycook@ucas.ac.cn (S.J.P.)

Outline

Supplementary Figure S1: Structural models, AFM and STEM characterizations of monolayer CrOCl

Supplementary Figure S2: Transformation of a CrOCl monolayer into a new square-lattice material revealed by STEM-ADF imaging

Supplementary Figure S3: Experimental and simulated STEM-ADF images and line intensity profiles across the interface between monolayer CrOCl and the newly formed square lattice crystal

Supplementary Figure S4: Low-magnification elemental mappings of the new square lattice crystal

Supplementary Figure S5: Quantitative EELS elemental analysis of a CrO_x monolayer

Supplementary Figure S6: STEM-ADF image of a CrOCl-CrO lateral heterojunction and the corresponding strain mapping

Supplementary Figure S7: Atomic-resolution STEM-ADF images of twisted CrOCl bilayers and as-fabricated twisted CrO bilayers

Supplementary Figure S8: FFT patterns of original twisted CrOCl bilayers and as-fabricated twisted CrO bilayers

Supplementary Figure S9: Two other moiré polymorphs for CrO bilayers with a 36.8° twist angle

Supplementary Figure S10: Experimental and simulated STEM-ADF images of two additional CrO commensurate moiré superlattices

Supplementary Figure S11: Band structure and anti-bonding state of monolayer CrOCl

Supplementary Figure S12: Transition mechanism from CrOCl to CrO and the interface structure model

Supplementary Figure S13: In-plane lattice expansion leading to nanostrip formation due to redundant Cr and O atoms

Supplementary Figure S14: Structural models of various chromium oxide monolayers

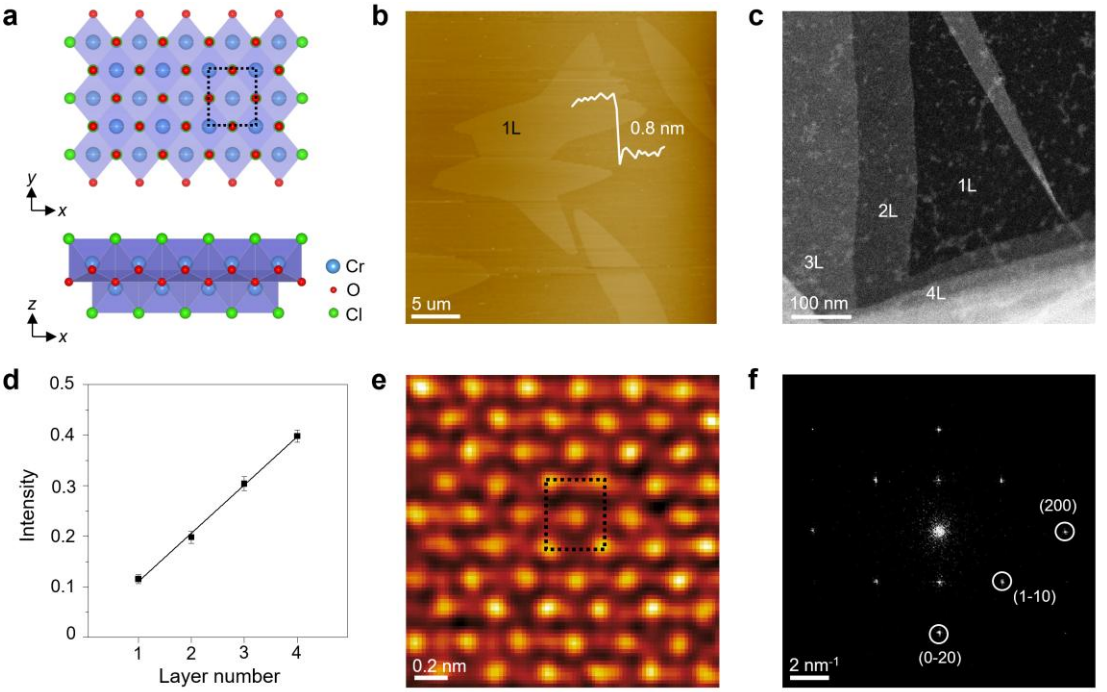

Figure S1 | Structural models, AFM and STEM characterizations of monolayer CrOCl. a, Relaxed in-plane and out-of-plane structural models of freestanding monolayer CrOCl. The top and side views show Cr atoms located at the centers of distorted octahedra formed by Cl and O atoms. The dashed rectangles in (a) and (e) indicate the unit cell of CrOCl. **b**, Representative atomic force microscopy (AFM) image of monolayer (1L) CrOCl films on mica substrates, acquired using a Bruker Multimode 8. The measured thickness of the 1L CrOCl (0.8 nm) aligns closely with the lattice constant (c = 0.795 nm). **c**, Low-magnification STEM-ADF image of a CrOCl specimen region containing monolayer (1L) to four-layer (4L). **d**, Intensities of 1L, 2L, 3L, and 4L CrOCl derived from (c), showing high linearity. **e**,**f**, Typical atomic-resolution STEM-ADF image (e) of a suspended CrOCl monolayer and fast Fourier transform (FFT) pattern (f), clearly illustrating the anisotropic orthorhombic in-plane structure. To minimize electron beam induced damage to CrOCl, imaging was performed at an electron dose rate of approximately 240 e^{-} Å^{-2} s^{-1}.

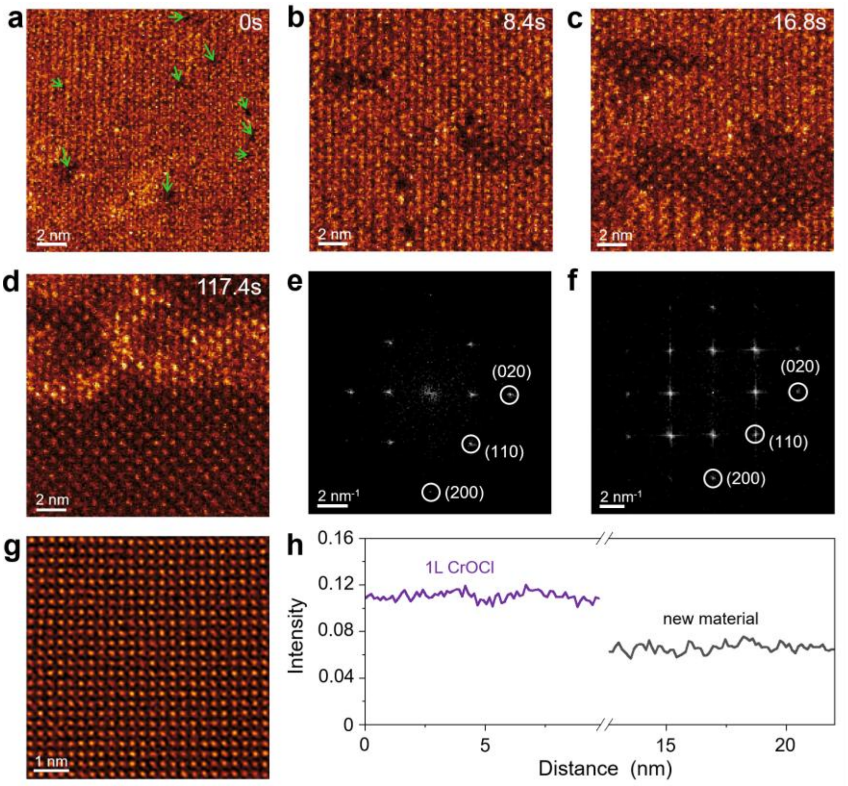

Figure S2 | Transformation of a CrOCl monolayer into a new square-lattice material revealed by STEM-ADF imaging. a-d, Time sequential atomic-resolution STEM-ADF images showing the transition of a CrOCl monolayer into a square-lattice material. In (a), green arrows highlight atomic defects induced by electron beam irradiation. The subsequent coalescence process, shown in panels (b-d), lead to the formation of a novel square lattice structure (d). **e**,**f**, FFT patterns of the STEM-ADF images (a) and (g), respectively, revealing a transformation from an orthorhombic CrOCl lattice to a square lattice. **g**, STEM-ADF image of the newly formed square lattice material. **h**, Line intensity profiles extracted from STEM-ADF images of the monolayer CrOCl and the fabricated new material, highlighting intensity differences. The STEM-ADF images were acquired under consistent experimental conditions.

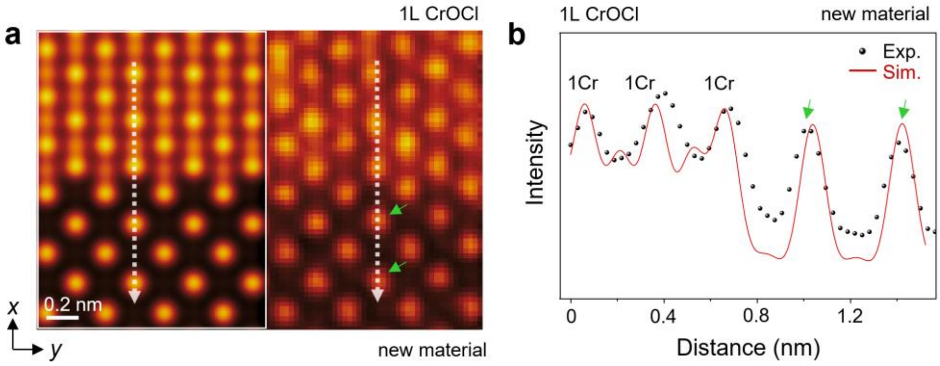

Figure S3 | Experimental and simulated STEM-ADF images and line intensity profiles across the interface between monolayer CrOCl and the newly formed square lattice crystal. a, Experimental and overlaid simulated atomic-resolution STEM-ADF images of the interface. The STEM-ADF images in (a) are reproduced from Fig. 2b in the main text. The image simulation was conducted using a model in which the upper portion represents a monolayer CrOCl, while the lower portion consists of a square lattice formed by single Cr atoms. **b**, Experimental and simulated line intensity profiles extracted along the dashed lines in (a), respectively. Green arrows indicate the atomic sites in the new square-lattice material, whose bright contrast closely align with those of the simulated single Cr atoms and the experimental single Cr atoms in monolayer CrOCl, confirming that these sites correspond to individual Cr atoms.

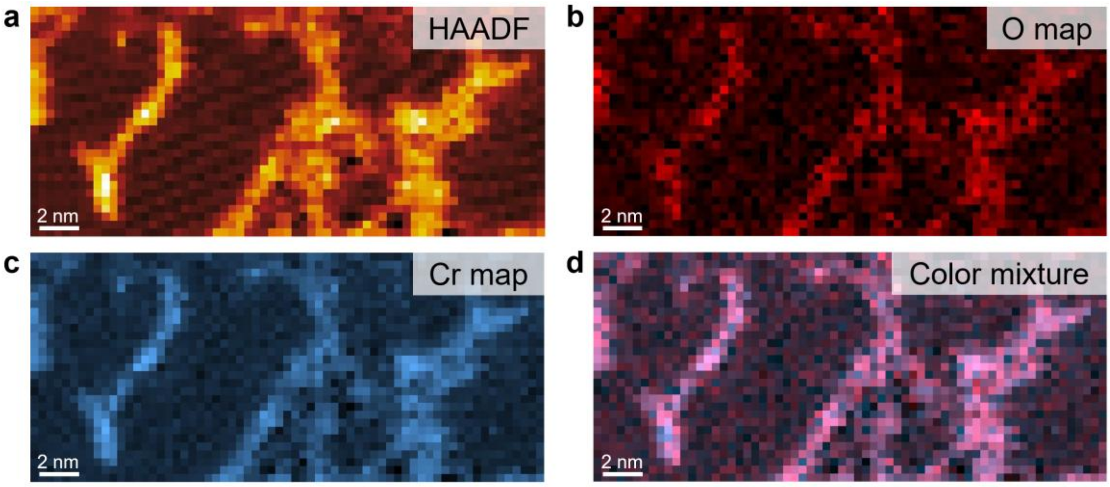

Figure S4 | Low-magnification elemental mappings of the new square lattice crystal. a, Low-magnification STEM-ADF image of the as-fabricated new material, acquired simultaneously with the core-loss EELS. The dark contrast in (a) corresponds to the new crystal, while the bright contrast belongs to nanostrips formed by excess Cr and O atoms during the transformation. **b-d**, Core-loss EELS mappings of O-K (b), Cr-$L_{2,3}$ (c) signals, and their color mixture map (d). Initial data processing for this dataset included the removal of noise spikes at 565.3 eV. No Cl signal was detected.

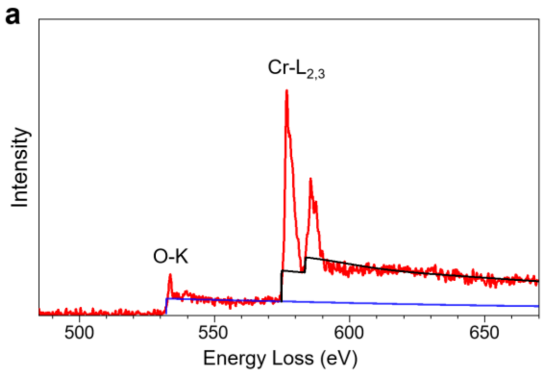

b

	Composition (at. %)
Cr	48 ± 3 %
O	52 ± 3 %

Figure S5 | Quantitative EELS elemental analysis of a CrO_x monolayer. a, Background-subtracted EEL spectrum of a CrO_x monolayer (red curve), alongside the Hartree–Slater cross-section profiles for O (blue line) and Cr (black line). **b**, Quantitative analysis results showing a Cr:O atomic ratio that is nearly 1:1.

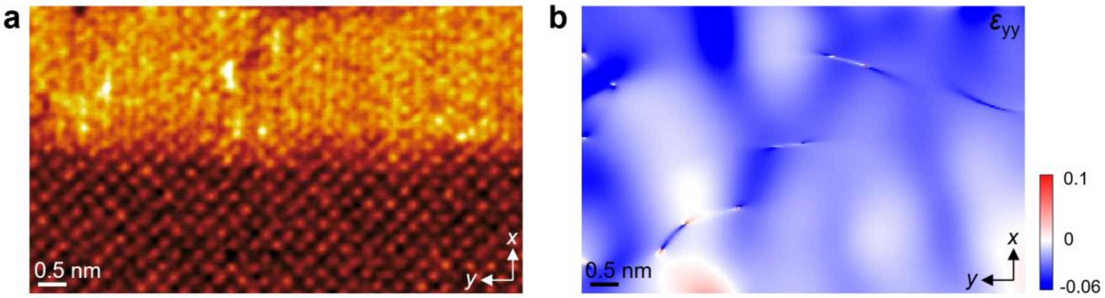

Figure S6 | STEM-ADF image of a CrOCl-CrO lateral heterojunction and the corresponding strain mapping. a, STEM-ADF image of a CrOCl-CrO heterojunction, which is identical to Fig. 2a in the main text. **b**, Corresponding strain mapping ε_{yy} along the *y* axis of CrOCl, showing no misfit dislocations.

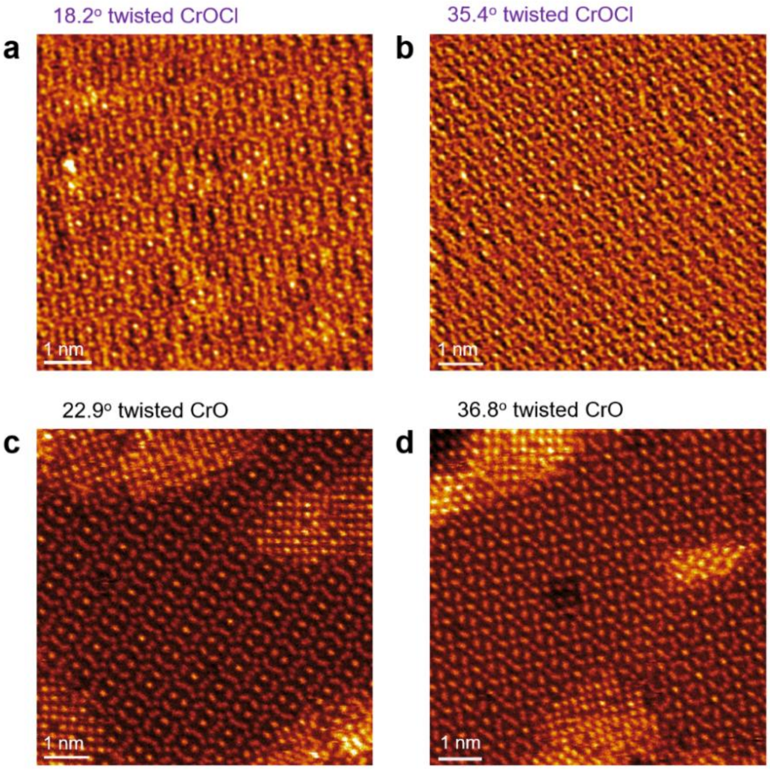

Figure S7 | Atomic-resolution STEM-ADF images of twisted CrOCl bilayers and as-fabricated twisted CrO bilayers. **a**,**b**, Atomic-resolution STEM-ADF images of the original CrOCl bilayers with twist angles of 18.2° (**a**) and 35.4° (**b**). **c**,**d**, STEM-ADF images of the fabricated CrO bilayers with twist angles of 22.9° (**c**) and 36.8° (**d**).

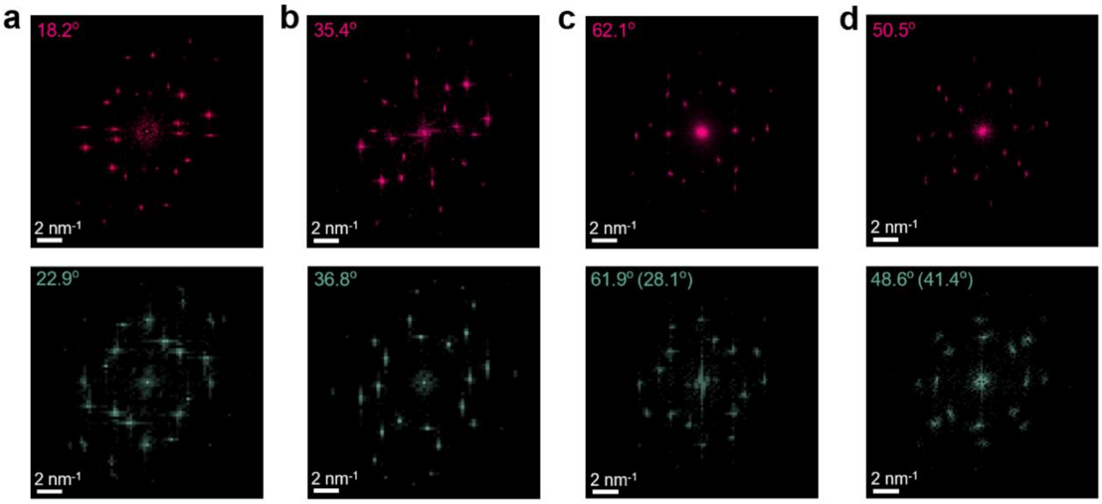

Figure S8 | FFT patterns of original twisted CrOCl bilayers and as-fabricated twisted CrO bilayers. a-d, FFT patterns of the original CrOCl twisted bilayers (pink) and the corresponding resulting CrO twisted bilayers (cyan). In these cases, the twist angle of the resulting CrO bilayer is either slightly larger (a,b), smaller (d) or nearly identical (c) to that of the initial CrOCl bilayer. Since CrO has a square lattice, the twist angle θ is equivalent to 90°-θ. Therefore, twist angles of 61.9° and 48.6° are equivalent to 28.1° and 41.4°, respectively. The four CrO bilayer twist angles, 22.9°, 36.8°, 61.9°(28.1°) and 48.6°(41.4°), correspond to $\sqrt{13}\times\sqrt{13}$, $\sqrt{5}\times\sqrt{5}$, $\sqrt{17}\times\sqrt{17}$, and $\sqrt{73}\times\sqrt{73}$ commensurate moiré superlattices, respectively.

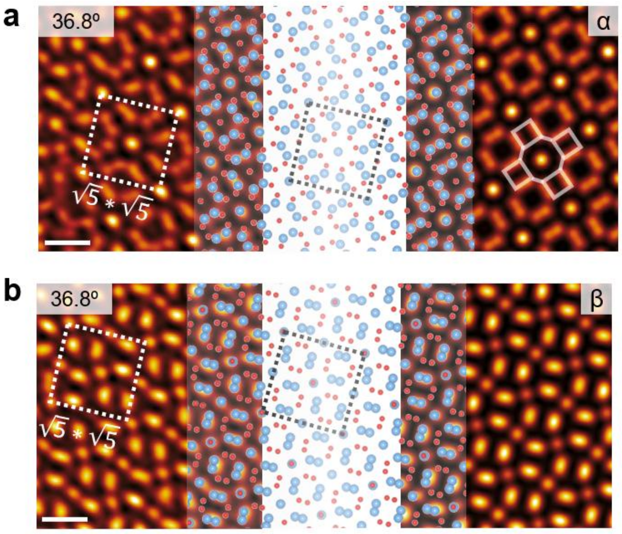

Figure S9 | Two other moiré polymorphs for CrO bilayers with a 36.8° twist angle.

a,b, STEM-ADF images of two other moiré polymorphs- α (a) and β (b) observed in 36.8° twisted CrO bilayers. Figure 2d in the main text depicts the γ polymorph. Each of them exhibits unique moiré patterns.

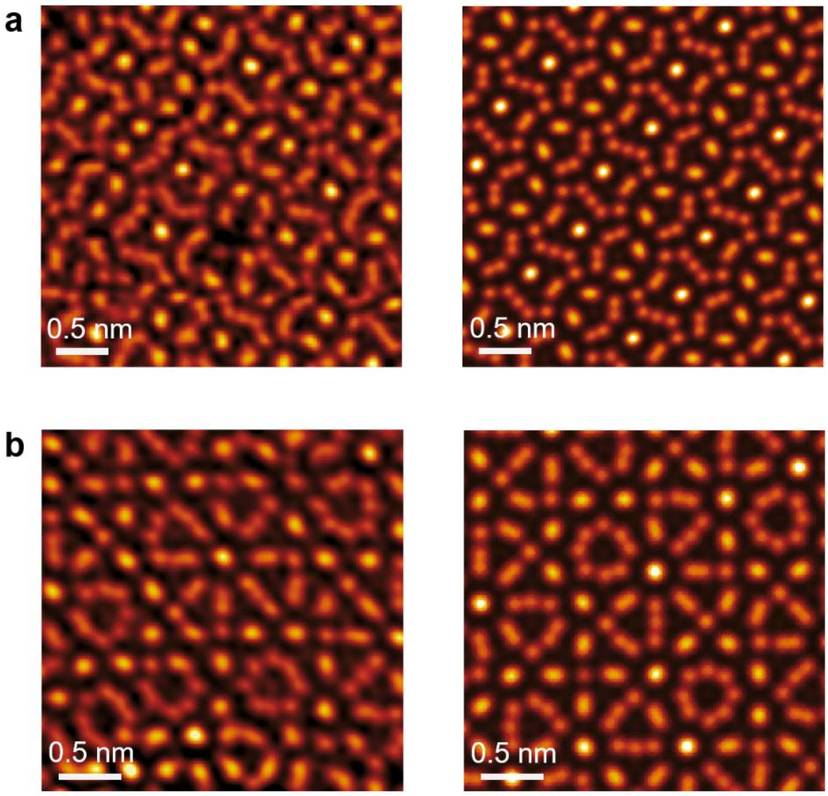

Figure S10 | Experimental and simulated STEM-ADF images of two additional CrO commensurate moiré superlattices. a, Experimental (left) and simulated (right) STEM-ADF images of the $\sqrt{17} \times \sqrt{17}$ CrO commensurate moiré superlattice with a 28.1° twist angle. **b**, Experimental (left) and simulated (right) STEM-ADF images of the $\sqrt{73} \times \sqrt{73}$ CrO commensurate moiré superlattice with a 41.4° twist angle. The simulated images here are based on rigidly twisted structural models.

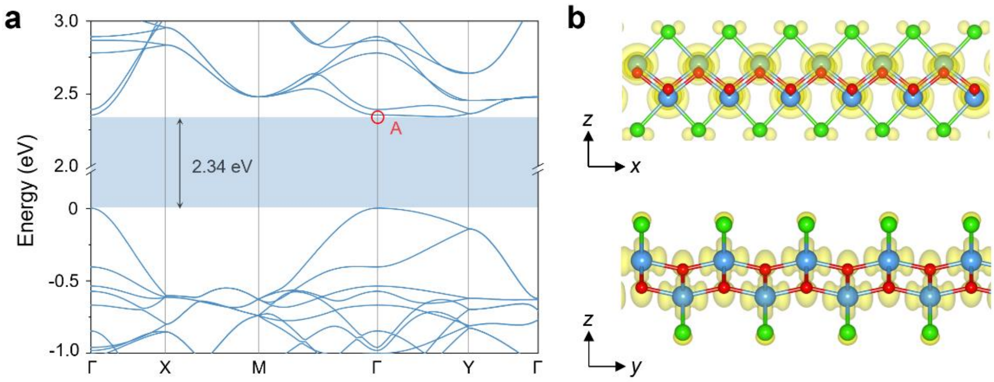

Figure S11 | Band structure and anti-bonding state of monolayer CrOCl. a, Band structure of monolayer CrOCl in its Néel antiferromagnet state, displaying a 2.34 eV bandgap. The red circle highlights the unoccupied state (A) at the Γ point. **b**, Side-view plots of the squared wavefunction norm of state A, indicating that state A is an anti-bonding state for both Cr-Cl and Cr-O bonds.

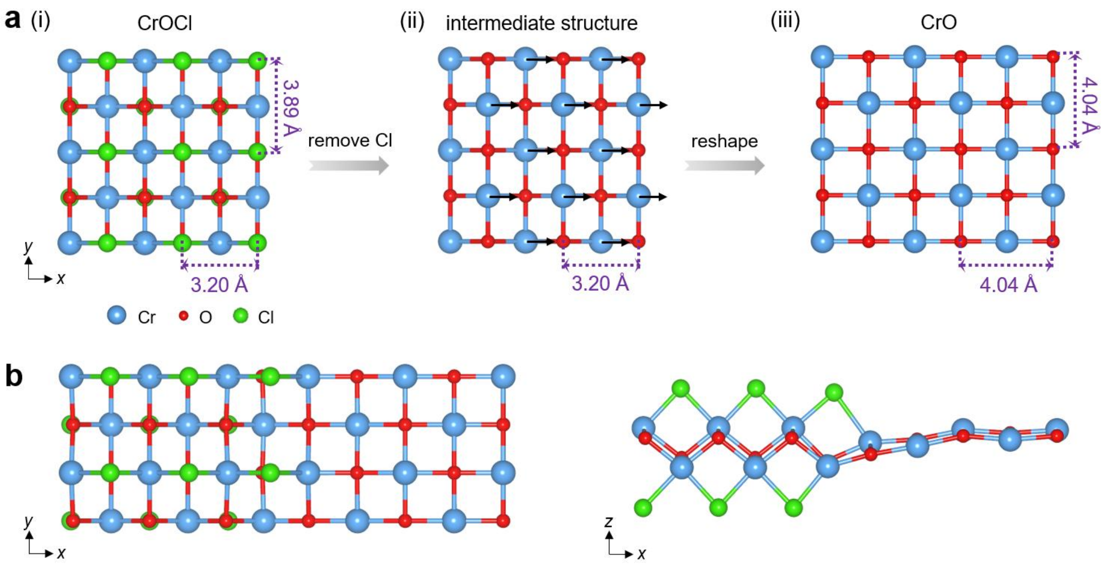

Figure S12 | Transition mechanism from CrOCl to CrO and the interface structure model. a, Top-view schematic of the transition from CrOCl to CrO. **b,** Relaxed structural models of the coherent CrOCl-CrO interface, shown from the top and side views.

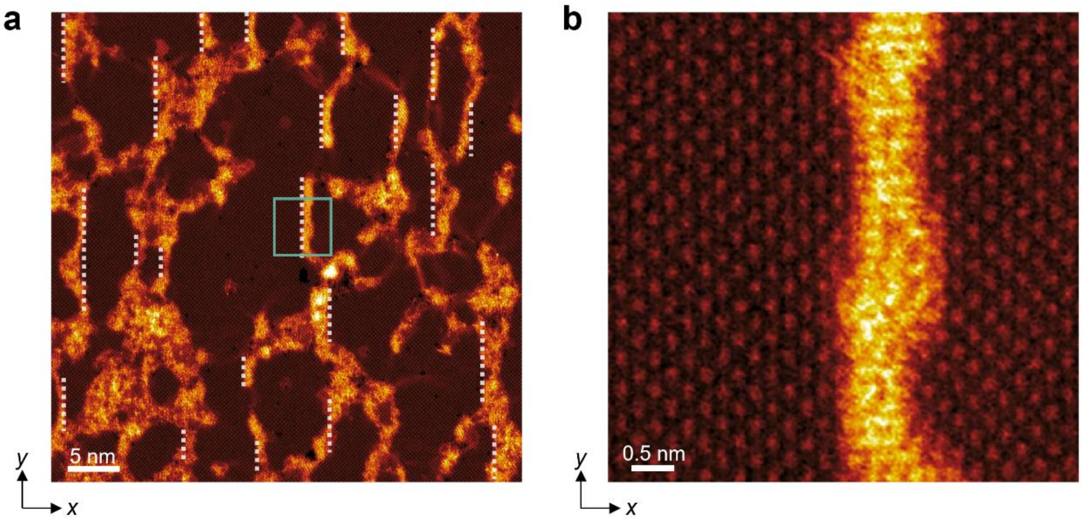

Figure S13 | In-plane lattice expansion leading to nanostrip formation due to redundant Cr and O atoms. a, Low-magnification STEM-ADF image showing the formed CrO membrane and CrO_x nanostrips. Most of the nanostrips are aligned along the *y* axis, as expected, perpendicular to the growth direction of CrO. The white dashed lines serve as guides to highlight the *y* axis direction. **b**, Close-up view of the region marked by the cyan square in (a), highlighting a CrO_x nanostrip that is highly aligned along the *y* axis.

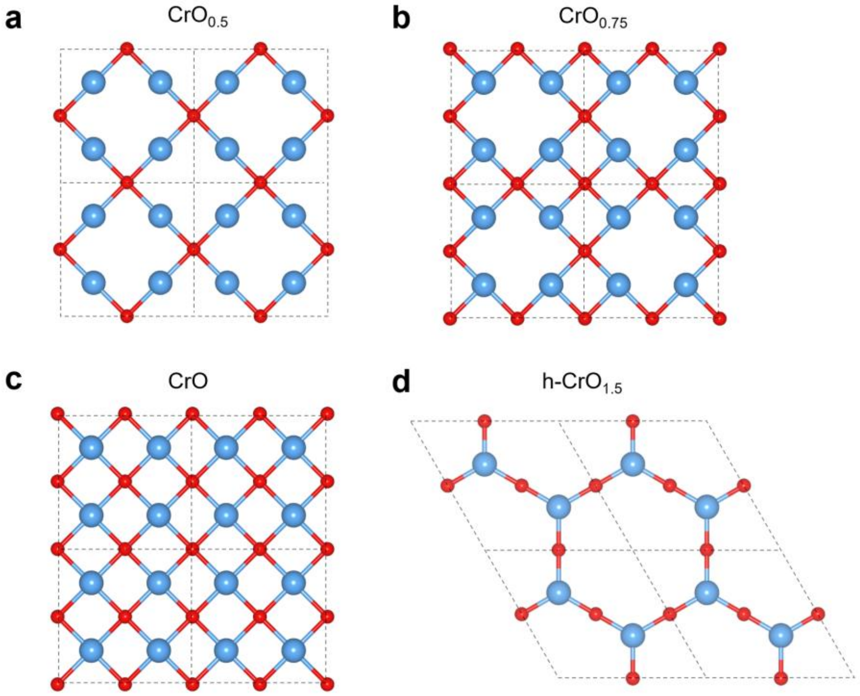

Figure S14 | Structural models of various chromium oxide monolayers. a-d, Relaxed structural models of $CrO_{0.5}$ (a), $CrO_{0.75}$ (b), CrO (c), and hexagonal Cr_2O_3 (h-$CrO_{1.5}$) (d) monolayers.

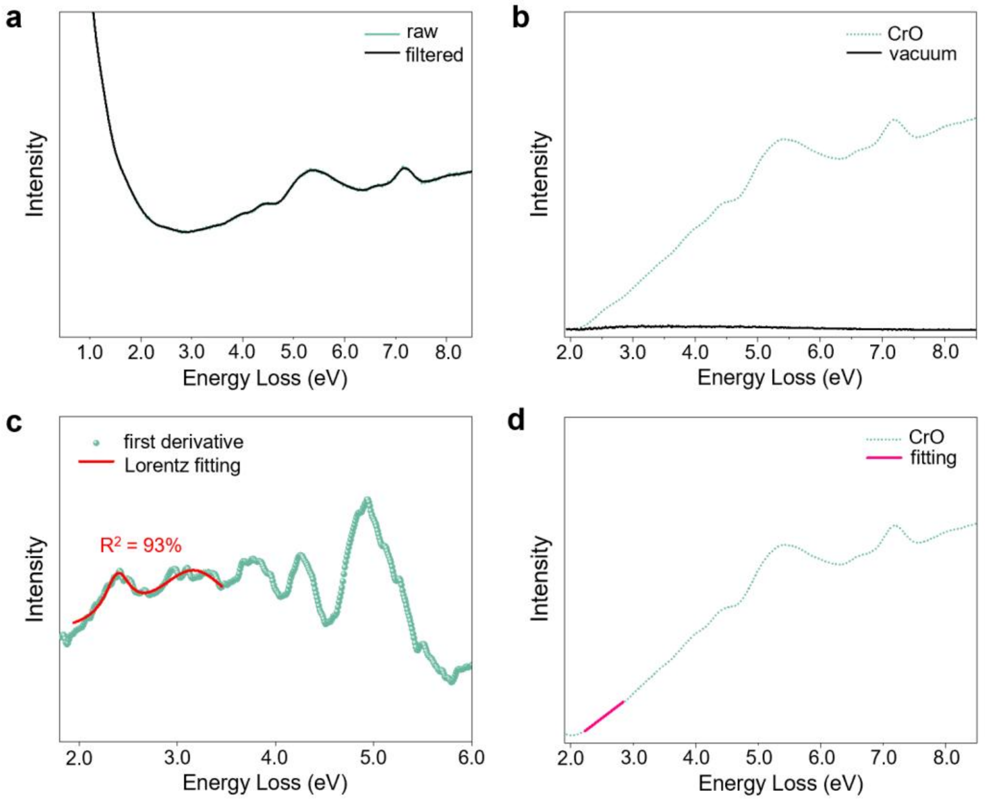

Figure S15 | Bandgap measurement of monolayer CrO. a, Experimental raw valence EEL spectrum of monolayer CrO (cyan curve), along with the corresponding spectrum after Savitzky-Golay filtering (black curve). **b**, Background subtracted CrO EEL spectrum (cyan dotted curve), compared with the reference spectrum collected at vacuum (black curve). **c**, First derivative of the CrO spectrum (cyan scatter plot) and the corresponding Lorentz fitting results (red curve) for the first and second positive peaks. The derived bandgap value, E_g, is 2.23 ± 0.18 eV. This figure is reproduced from the inset of Fig. 3f. **d**, CrO spectrum (cyan dotted curve) and the fitting result of E_g = 2.14 eV (pink line) obtained using the tangent method.

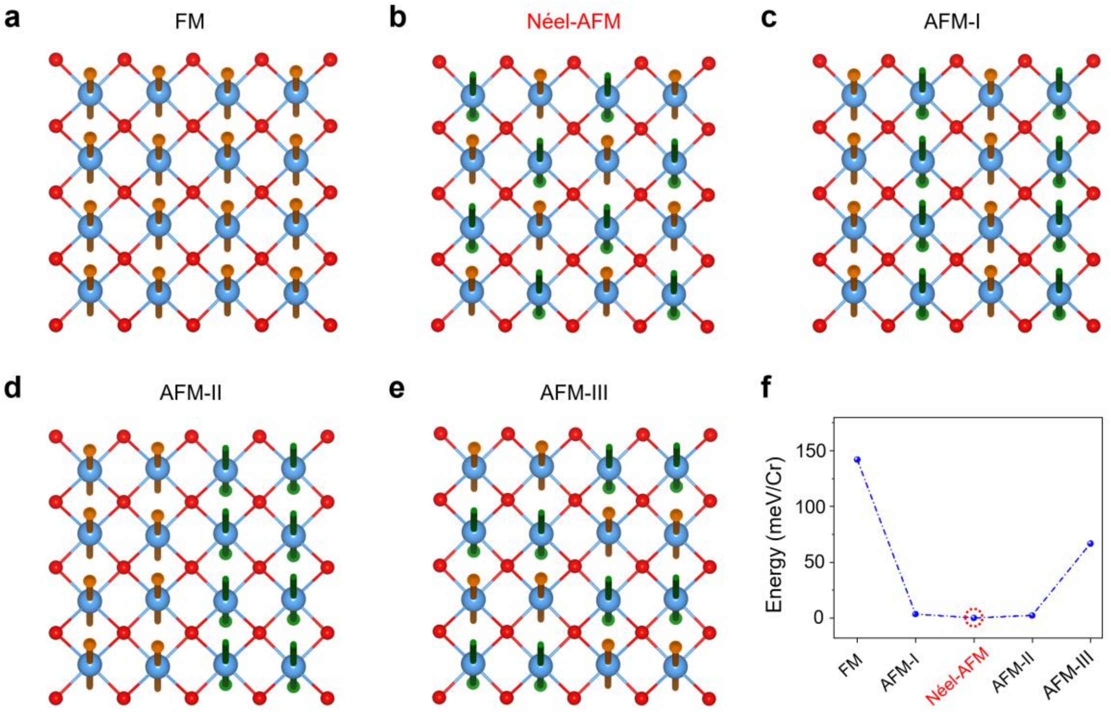

Figure S16 | Magnetic orders of monolayer CrO and their energies. a-e, Schematic representations of five magnetic configurations of monolayer CrO, including one ferromagnetic (FM) configuration and four antiferromagnetic (AFM) configurations: Néel-AFM, AFM-I, AFM-II, and AFM-III. The Néel-AFM order in (b) corresponds to the configuration shown in Figure 3g in the main text, viewed from a different perspective. **f**, Energies of the various magnetic configurations, with the Néel-AFM order identified as the ground state.

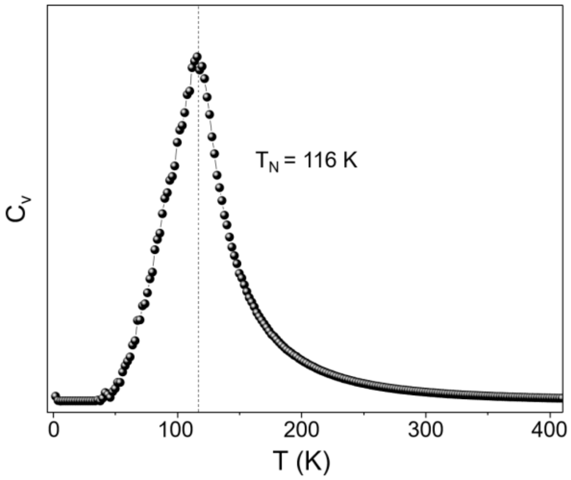

Figure S17 | Temperature dependence of the constant-volume heat capacity of monolayer CrO. The critical temperature, T_N, is estimated to be 116 K.

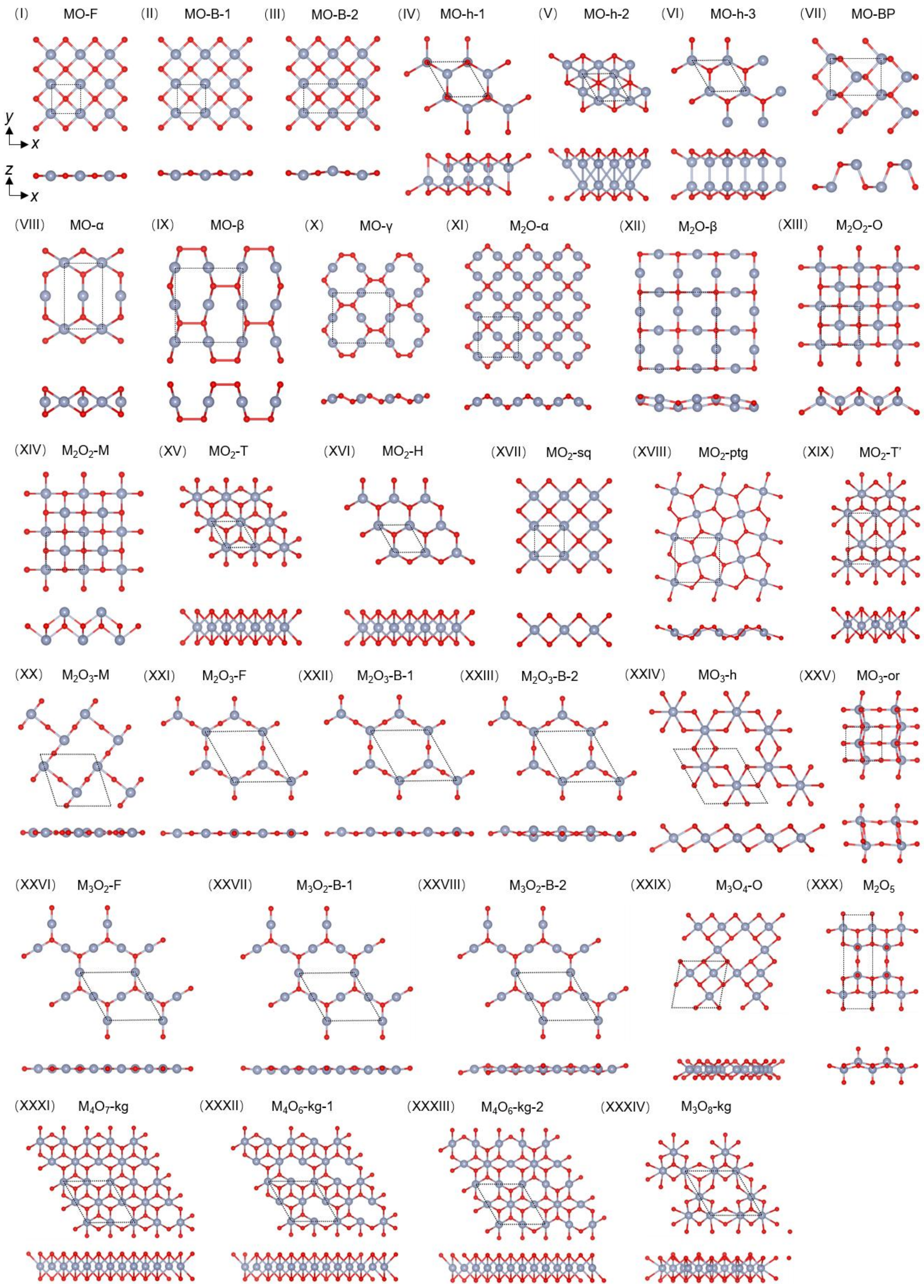

Figure S18 | 34 distinct freestanding monolayer metal oxide structures considered in high-throughput calculations. The abbreviation “F”, “B”, “h”, “BP”, “or”, “ptg” and “kg” mean “flat”, “buckled”, “hexagonal”, “black phosphorous”, “orthorhombic”, “pentagon” and “Kagome”, respectively. The black dashed rectangles, squares and rhombuses indicate the unit cells.

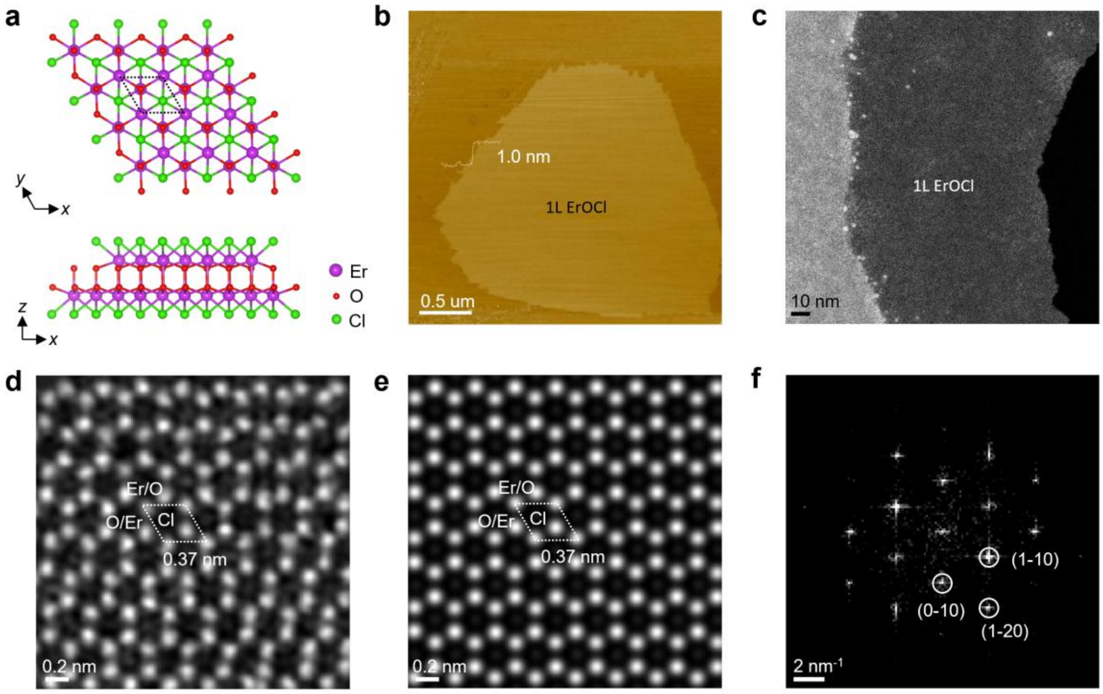

Figure S19 | Structure models, AFM and STEM characterizations of monolayer ErOCl. a, In-plane and out-of-plane structural models of monolayer ErOCl. Dotted rhombuses in (a) and (d-e) denote the unit cell. **b,** AFM image of monolayer ErOCl on a mica substrate, showing a measured thickness of 1.0 nm, consistent with the monolayer value (c = 0.92 nm). **c,** Low-magnification STEM-ADF image of a freestanding ErOCl monolayer. **d,e,** Experimental (d) and simulated (e) atomic-resolution STEM-ADF images of single-layer ErOCl. The simulation reproduces the experimental image. **f,** Representative FFT pattern graph of ErOCl.

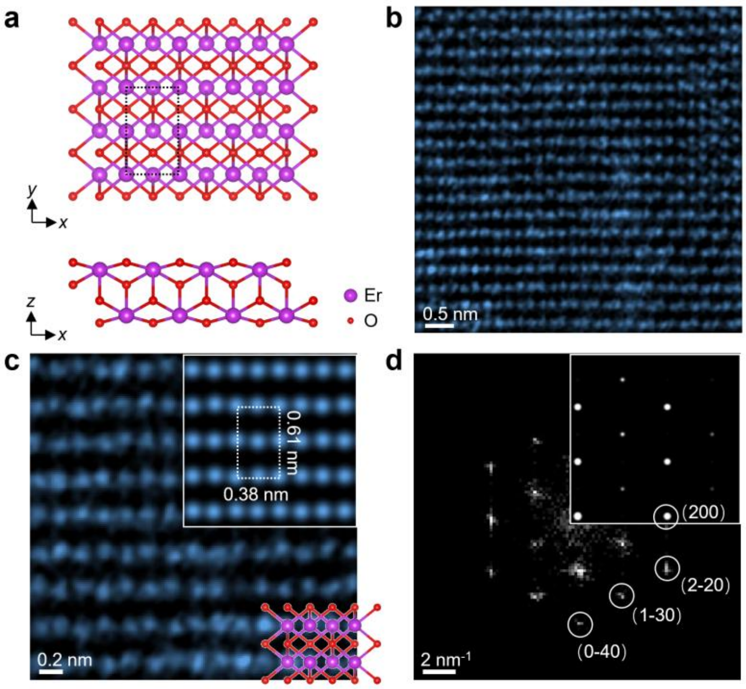

Figure S20 | Experimental and simulated STEM images and FFT patterns of ErO. **a,** Structural models of monolayer ErO viewed from top and side, which are reprodeced from Fig. 4e in the main text. **b,** Atomic STEM-ADF image of a synthesized ErO monolayer. **c,** Magnified STEM-ADF image, displaying a rectangular lattice. Insets show the corresponding simulated image and overlaid structural model. The dotted rectangles in (a) and (c) indicate the unit cell. The STEM-ADF image in (c) is reproduced from Fig. 4f in the main text. **d,** Experimental FFT pattern of ErO, consistent with the simulated pattern shown in the inset.

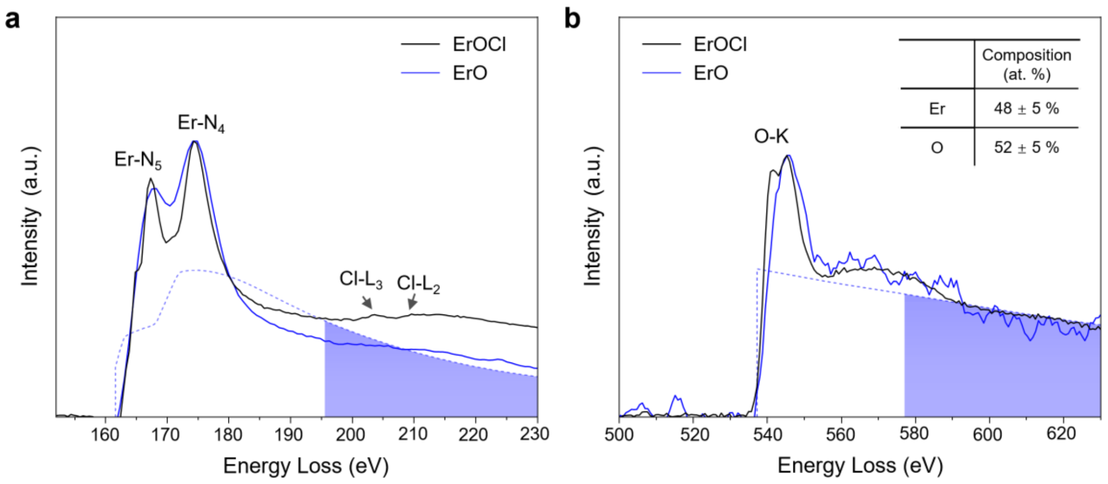

	Composition (at. %)
Er	48 ± 5 %
O	52 ± 5 %

Figure S21 | Quantitative EELS elemental analysis of a ErO monolayer. a, Background-subtracted EEL spectra acquired from monolayer ErOCl (black solid line) and ErO (blue solid line). In contrast to ErOCl, the Cl-$L_{2,3}$ signal is absent in the ErO spectrum, indicating the removal of Cl. **b,** Core-loss EELS O-K edges of ErOCl (black solid line) and ErO (blue solid line). The blue dashed curves in (a) and (b) represent Hartree-Slater cross-section profiles for Er and O, respectively. The energy ranges in blue were fitting regions used to quantify Er:O atomic ratio, which is close to 1:1. The EEL spectra were smoothed using a Savitzky-Golay filter.

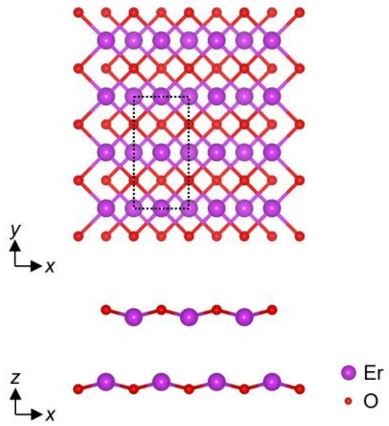

Figure S22 | In-plane and out-of-plane structural models of freestanding ErO. The dashed rectangle indicates the unit cell of freestanding ErO.

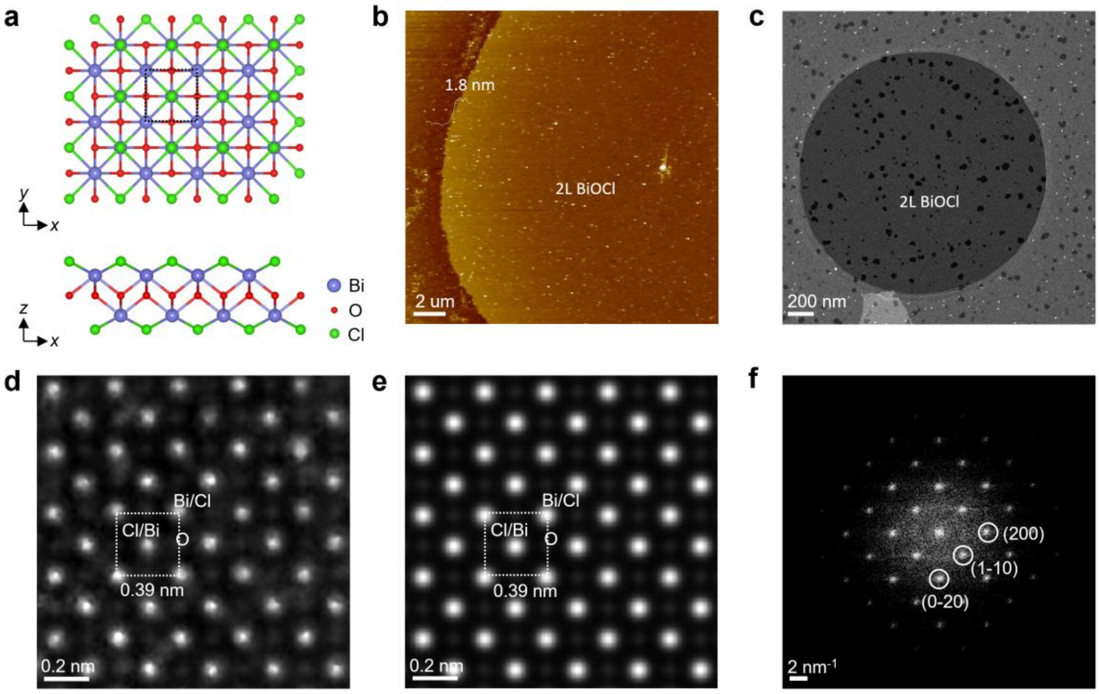

Figure S23 | Structural models, AFM and STEM characterization of bilayer BiOCl. **a,** In-plane and out-of-plane structural models of BiOCl. The dotted squares in (a) and (d-e) indicate the unit cell. **b,** Representative AFM image of bilayer BiOCl on mica substrates. The measured thickness (1.8 nm) matches the expected value for a bilayer BiOCl (c = 0.74 nm). **c,** Low-magnification STEM-ADF image of a freestanding bilayer BiOCl membrane. **d,e,** Experimental (d) and simulated (e) phase images of AA-stacked bilayer BiOCl. The experimental image was reconstructed from a 4D-STEM dataset. In (d–e), bright contrast correspond to Bi/Cl columns, and dim contrast represent O columns. The simulated image shows high agreement with the experimental result. **f,** Representative FFT pattern of BiOCl.

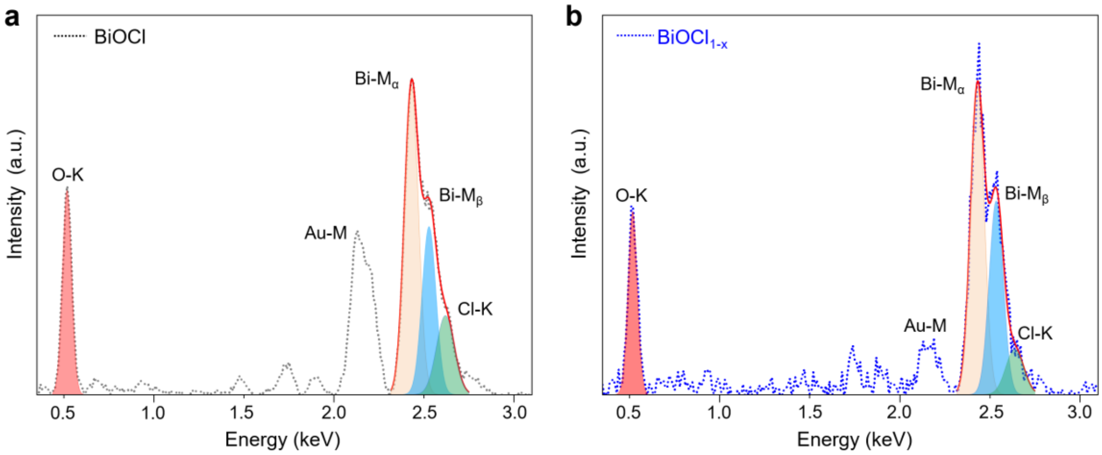

Figure S24 | EDS elemental analysis of pristine BiOCl and $BiOCl_{1-x}$ membranes. **a,** EDS spectrum of a pristine BiOCl film acquired under low magnification to minimize beam-induced damage. **b,** EDS spectrum of $BiOCl_{1-x}$ membranes (see Supplementary Fig. S25b) formed under electron beam irradiation. The red, orange, blue, and green Gaussian peaks in (a-b) represent fittings for O-K, Bi-M_{α}, Bi-M_{β} and Cl-K signal, respectively. Compared to pristine BiOCl, the Cl-K signal in the $BiOCl_{1-x}$ spectrum is significantly reduced but nonzero. The Bi:O atomic ratio remains close to 1:1, as indicated by similar O-K to Bi-M intensity ratios in both BiOCl and $BiOCl_{1-x}$ spectra.

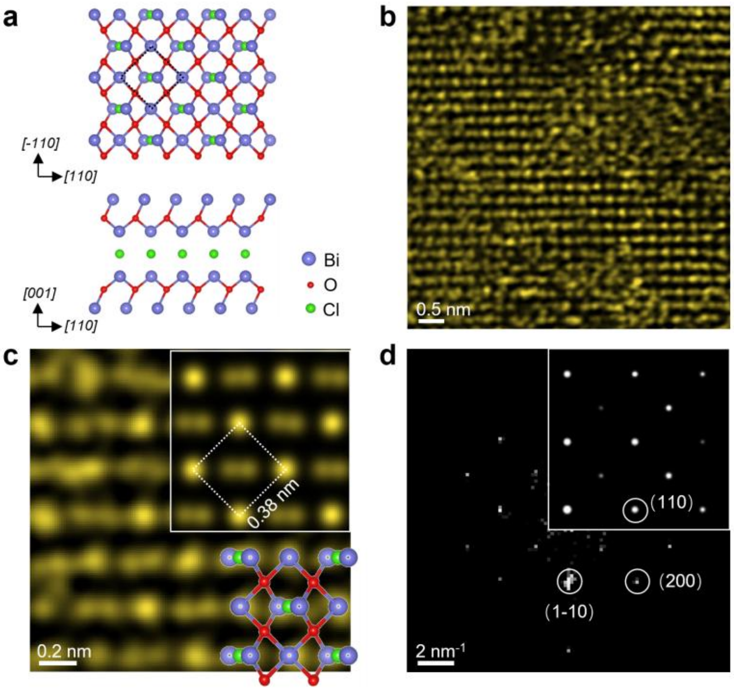

Figure S25 | Experimental and simulated STEM images and FFT patterns of $\mathbf{Bi_4O_4Cl}$. a, Top and side views of relaxed structural models of Bi_4O_4Cl. This structure can be interpreted as a Bi_2O_2-M bilayer intercalated with Cl atoms. **b,** Atomic-resolution STEM-ADF image of the synthesized Bi_4O_4Cl. **c,** Enlarged region from (b) revealing a square-lattice structure with central Bi-Bi dimers. Dotted squares in (a) and (c) indicate the unit cell. Insets present the corresponding simulated image and the structural model used for simulation. The STEM-ADF image in (c) is reproduced from Fig. 4h in the main text. **d,** Experimental FFT pattern of Bi_4O_4Cl, which agrees well with the simulated pattern shown in the inset.

Supplementary Note 1: Estimation of threshold kinetic voltages for atoms in monolayer CrOCl

The knock-on effect involves direct momentum transfer from incident electrons to atoms, which becomes significant only when the kinetic energy of the electrons exceeds a certain threshold required for disrupting a specific chemical bond[1]. In our molecular dynamics simulations, the incident electrons traveled from the upper to the lower sublayer of CrOCl. The threshold kinetic energies (E_e) for atoms in monolayer CrOCl were >63 keV for Cl atoms in the bottom sublayer, > 200 keV for Cl atoms in the upper sublayer, and > 200 keV for O atoms. Cl atoms in the upper sublayer collide with the atoms beneath to leave the CrOCl monolayer, while those in the bottom sublayer can depart from the layer much more easily[2]. This explains the higher E_e for Cl atoms in the upper sublayer compared to that for Cl atoms in the bottom sublayer. In our experiments, the acceleration voltage was set to 60 kV. Consequently, the knock-on effect alone is insufficient to remove all Cl atoms from the CrOCl structure, emphasizing the crucial role of the ionization effect.

References

1 Egerton, R. F. Radiation damage to organic and inorganic specimens in the TEM. *Micron* **119**, 72-87 (2019).

2 Pan, Y. *et al.* Selective linear etching of monolayer black phosphorus using electron beams. *Chin. Phys. B* **29**, 086801 (2020).